Motion Estimation with Finite-Element Biomechanical Models and Tracking Constraints from Tagged MRI

Arnold D. Gomez, Fangxu Xing, Deva Chan, Dzung L. Pham, Philip Bayly, and Jerry L. Prince

1 Introduction

Soft tissue deformation elicits vital transport processes throughout the body, and is a key determinant in widespread conditions and diseases. For example, systemic circulatory deficiencies may arise from impaired myocardial contraction, and acceleration-induced axonal overstretching has been linked to traumatic brain [1, 2] and can be investigated using MRI. Thus, noninvasive motion estimation is of clinical and investigational interest. However, the acquisition and processing of tagged MRI has been problematic due to long scan times, artifacts, and challenges in obtaining accurate 3D estimates of displacement and strain. It has been shown that integration of an organ's geometry (and fiber orientations if relevant) and use of material constitutive information can increase estimation accuracy, reduce artifacts, and improve one's ability to estimate dense displacements and strains from sparsely acquired imaging data [1, 3].

Motivated by versatile contrast and unparalleled soft tissue sensitivity, several motion estimation approaches have been developed within the MRI framework,

A.D. Gomez (✉) • J.L. Prince
Electrical and Computer Engineering Department, Johns Hopkins University, Baltimore, MD, USA
e-mail: adgomez@jhu.edu

F. Xing
Department of Radiology, Massachusetts General Hospital/Harvard Medical School, Boston, MA, USA

D. Chan • D.L. Pham
Center for Neuroscience and Regenerative Medicine, The Henry M. Jackson Foundation, Bethesda, MD, USA

P. Bayly
Mechanical Engineering Department, Washington University in St. Louis, St. Louis, MO, USA

A. Wittek et al. (eds.), *Computational Biomechanics for Medicine*,
DOI 10.1007/978-3-319-54481-6_7

as well as dedicated motion encoding pulse sequences, image postprocessing, or both [4]. Analysis of tagged MRI is one of the most well-established approaches which, from early implementations targeting the cardiovascular system, has expanded to include other organs [5–7].

Best results in 3D motion estimation generally require consistent repetition of movement and relatively high resolution, but these are constrained by scan time [8, 9]. Traditionally, displacement information has been reconstructed in the imaging planes first and then propagated to a 3D domain with the help of interpolation methods, such as splines, or finite elements [3, 10]. These approaches enable preemptive reduction of artifacts via smoothing or refinement, and enforce incompressibility during the interpolation process [10]. However, the imaging raster rarely aligns with the geometry or fiber structure of an organ; thus, smoothing or interpolation may introduce fictitious edge tractions, or violate other mechanical characteristics such as tissue anisotropy.

In this research, the tracking process is realized by enforcing image phase conservation in material points within the field of view (FOV), but not coincident with the spatial imaging raster. The proposed tracking kernel is based on the classic harmonic phase (HARP) analysis of tagged MRI [11], combined with hyperelastic model registration methods [1], according to a phase conservation principle parallel to intensity conservation in optical flow [12]. Thus, the results are *mechanically representative,* in that they are diffeomorphic, have traction free surfaces, and are otherwise consistent with continuum mechanics, but the phase vector formulation increases sensitivity in texture-free regions, and provides a more objective similarity metric.

We demonstrate our implementation in three scenarios. The first two consist of forward displacement reconstruction where the goal is to obtain deformation fields. These include: measurement of impact-induced deformation in a Sylgard™ brain phantom and quantification of fiber strain in residually stressed myocardium. The third scenario consists of displacement-based inverse parameter identification of intrinsic tongue muscle activation. Our results indicate that, in forward displacement reconstruction, the approach is robust to artifacts (edges and large displacements) and to material stiffening due to residual stress. In the inverse problem, we show that evaluating fiber stretch enables approximation of muscle activation without the need for iterative minimization.

2 Background

2.1 Harmonic Phase Analysis

Tagged MRI contains artificial magnetic patterns (lines or sinusoidal profiles) that are imposed near the beginning of a CINE sequence and deform with moving tissue. HARP analysis focuses on harmonic peaks in the Fourier domain, which arise from

the periodic nature of tag patterns. The harmonic phase vector, $\boldsymbol{\phi} = [\phi_1 \ \phi_2 \ \phi_3]^T$, where each term is the phase of the inverse Fourier transform of a harmonic peak in an image whose tag direction is orthogonal to the other two directions, carries information about local components of tissue motion. In particular, the phase at a reference location, $\boldsymbol{X}$, at $t = t_0 = 0$ will be the same as tissue moves to a new spatial location, $\boldsymbol{x}$, at a later time. In other words,

$$\boldsymbol{\phi}\,(\boldsymbol{X}, t_0) = \boldsymbol{\phi}\,(\boldsymbol{x}, t)\,. \tag{1}$$

Thus, 3D motion estimation can be thought of as the solution of a multidimensional, nonlinear, root-finding problem: given phase distributions at two time points, find $\boldsymbol{x}$ for a given $\boldsymbol{X}$, or vice versa.

We note that a practical application of HARP analysis deals not with the true real-valued phase, but rather with the *harmonic phase* whose range is the interval $[-\pi\,, \pi)$. Nevertheless, it is possible to use the expressions herein without loss of generality by adopting local phase unwrapping in the final implementation [11].

2.2 Deformations in Continuum Mechanics

Tissue deformation can be modeled as a boundary problem seeking to minimize an energy functional $E(\boldsymbol{\varphi})$, where the deformation map $\boldsymbol{\varphi}$ contains admissible deformations evaluated at material points, i.e., $\boldsymbol{\varphi}(\boldsymbol{X}) = \boldsymbol{x} = \boldsymbol{X} + \boldsymbol{u}(\boldsymbol{X})$ [1]. Given an integration domain, $\mathcal{R} \in \mathbb{R}^3$, the Euler–Lagrange equations necessary to minimize E are obtained by taking the directional derivative with respect to a small variation (or virtual displacement) in the spatial coordinates. This yields the weak form of the so-called virtual work equation,

$$\delta W = \int_{\mathcal{R}} \boldsymbol{P} : \delta \dot{\boldsymbol{F}}\, dV - \int_{\mathcal{R}} \boldsymbol{f}_0 \cdot \delta \boldsymbol{v}\, dV + \int_{\mathcal{S}} \boldsymbol{t}_0 \cdot \delta \boldsymbol{u}\, dS. \tag{2}$$

At equilibrium, $\delta W = 0$ describes a static momentum balance between body or boundary forces (respectively $\boldsymbol{f}_0$ and $\boldsymbol{t}_0$), and internal stresses defined by the material-dependent first Piola–Kirchhoff stress tensor, $\boldsymbol{P}(\boldsymbol{F})$, and the spatial gradient of the deformation map, $\boldsymbol{F} = \frac{d\boldsymbol{x}}{d\boldsymbol{X}}$ [13, 14].

One of the most popular approaches for solving the boundary problem associated with (2) is FE analysis. This process generally involves extracting discretized geometry from MRI via delineation and meshing, assigning a suitable constitutive model, and defining boundary conditions. The FE method has experienced considerable expansion in biomechanics, thanks to several improvements geared to handle complex biological geometries, and nonlinear material models [13, 15].

3 Tracking Tagged MRI with Deformable Models

3.1 Conservation of Harmonic Phase Vector

The basis of HARP analysis, (1), can also be described through physical conservation principles. Let $\boldsymbol{\phi}$ represent a vectorial angular quantity (per unit mass), which is conserved. Then, the net change in phase density can be expressed as a mass transport process defined in weak form by

$$\frac{D}{Dt}\int_{\mathcal{R}} \boldsymbol{\phi}\rho \, dV = \int_{\mathcal{R}} \frac{\partial (\boldsymbol{\phi}\boldsymbol{\rho})}{\partial \boldsymbol{t}} \, dV + \int_{\mathcal{S}} \rho\boldsymbol{\phi} \otimes \boldsymbol{v} \cdot \boldsymbol{n} \, dS, \tag{3}$$

where the right-hand side contains generative and advection terms dependent on mass density ρ and velocity $\boldsymbol{v}$ across a boundary surface with local normal $\boldsymbol{n}$ [16]. Application of Gauss' theorem and the continuity equation reduces the phase conservation relationship to

$$\frac{D\boldsymbol{\phi}}{Dt} = \frac{\partial \boldsymbol{\phi}}{\partial \boldsymbol{t}} + \nabla \boldsymbol{\phi} \cdot \boldsymbol{v}. \tag{4}$$

The left side of the equation corresponds to the material description, which yields the deformable model tracking constraint discussed in the next section. The middle expression is equivalent to the spatial description, and is the harmonic phase equivalent of the familiar optical flow equation used in intensity-based image registration [12].

3.2 Nonlinear Tracking Constraint

We now focus on obtaining displacements using the material description of harmonic phase conservation noting that direct application of (1) has two key limitations: First, harmonic phase vector pairs are not unique as a consequence of phase wrapping, thus tracking may converge at erroneous locations after large displacements; second, without regularization, tracking points near edges will result in spurious displacements due to partial volume artifacts.

Definition

Using integration with respect to time, the total derivative in (4) can be formulated as a difference between two phase images, acquired at the reference and at a subsequent time, evaluated at a material point and its corresponding location in the deformed configuration, i.e., $\boldsymbol{x} = \boldsymbol{x}(\boldsymbol{X}, t)$. This difference defines the nonlinear tracking constraint to be imposed on (2),

$$\boldsymbol{f}_{harp} = \lambda(t)\left(\boldsymbol{\phi}\left(\boldsymbol{x}\left(\boldsymbol{X},\boldsymbol{t}\right),\boldsymbol{t}\right) - \boldsymbol{\phi}\left(\boldsymbol{X},\boldsymbol{t}_0\right)\right), \tag{5}$$

where $\lambda(t)$ is a Lagrange multiplier that enforces phase consistency in tracking. In essence, the constraint introduces an additional body force whose purpose is to deform the model according to the temporal changes in the tag patterns.

Implementation

Given the nonlinear nature of (5), implementation within a Newton–Raphson (or similar) iterative solver requires consistent linearization of the virtual work contribution from the constraint to be applied on (2). In other words, linearizing $\delta W_{\text{harp}}\left(\boldsymbol{x},\delta\boldsymbol{v}\right) = \int_{\mathcal{R}} \boldsymbol{f}_{\text{harp}}\cdot\delta\boldsymbol{v}\, dV$ yields the tangent stiffness aggregate to be passed along to the solver, i.e.,

$$D\delta W_{harp}\left(\boldsymbol{x},\delta\boldsymbol{v}\right)[\boldsymbol{u}] = \int_{\mathcal{R}} \lambda(t)\nabla\boldsymbol{\phi}\left(\boldsymbol{x}\left(\boldsymbol{X},\boldsymbol{t}\right),\boldsymbol{t}\right)\ \delta\boldsymbol{v}\cdot\delta\boldsymbol{u}\, dV. \tag{6}$$

The tracking constraint was implemented as a plug-in extension to the FE solver within the FEBio Software Suite [15].

Image Preprocessing

In (5), it is assumed that the harmonic phase images are defined everywhere, which typically is not the case. Therefore, an image interpolation step must be built into the implementation. In fact, we propose upsampling tagged images prior to harmonic peak extraction (effective bandwidth remains limited by the original acquisition). We used grid-based cubic spline interpolation to achieve isotropic resolution based on the in-plane slice resolution. As with conventional HARP analysis, band-pass filtering is necessary to extract harmonic peaks. In this research, each 2D slice was filtered one image at a time, with a circular band-pass filter centered at the tagging frequency with a radius equal to half of the center frequency [11].

Solution Strategy

Two main approaches for enforcement of tracking constraints are available in this implementation. The first consists of applying a global, linearly increasing, penalty $\lambda(t)$ function (penalty method), and the second consists of using an iterative approximation to its local values to a given tolerance (augumented Lagrangian) [17]. Both the maximum penalty $\lambda_{\max}$ and tolerance λ_{tol} were adjusted according to a desired tracking residual $\varepsilon = \int \boldsymbol{\phi}(\boldsymbol{x}(\boldsymbol{X},t),t) - \boldsymbol{\phi}(\boldsymbol{X},t_0)\, dV$.

4 Experiments and Results

4.1 Measuring Impact-Induced Deformation in Brain Phantom

The goal of this experiment was to demonstrate our approach against traditional HARP analysis, i.e., application of (1) with a fixed-point algorithm, for reconstructing the motion of a Sylgard™ phantom, Fig. 1(a). The phantom's base was subject to a sudden rotational acceleration and consequently imaged (3T scanner, 13 frames, 18 ms TR, 13 axial slices, 160 ×160 px, 1.5 ×1.5 mm, SPAMM sequence). Two FE models of the phantom were constructed: one consisting of 4250 linear (fully integrated) brick elements, and the other used the same number of elements using a quadratic 20-node formulation. In both, the material was modeled as a Neo-Hookean solid ($C_1 = 1.0$ kPa, $\kappa = 120$ kPa). Tracking was performed to $\varepsilon = 0.05$ rad, with $\lambda_{\max} = 0.2$, and $\lambda_{\text{tol}} = 0.1$. Both algorithms ran for ten iterations per time frame.

Representative displacements at $t = 54$ ms appear in Fig. 1(c) and (d), for conventional HARP and our method, respectively. As expected, using a fixed-point algorithm results in two types of artifacts: spurious displacements near the edges, and erroneous tracking due to large displacements. In contrast, the proposed methodology results in smooth (traction-free) displacements at the boundaries, and consistent tracking of rotation. Both linear and quadratic meshes yielded identical qualitative results with minor quantitative differences (less than 0.1%).

4.2 Quantifying Fiber Stretch in Residually Stressed Myocardium

Most tissues, even in the absence of loading, exhibit some level of residual stress, which becomes apparent by recoil following an incision, suggesting that fibers in situ are prestretched [18]. Here, we (a) demonstrate that our approach may include

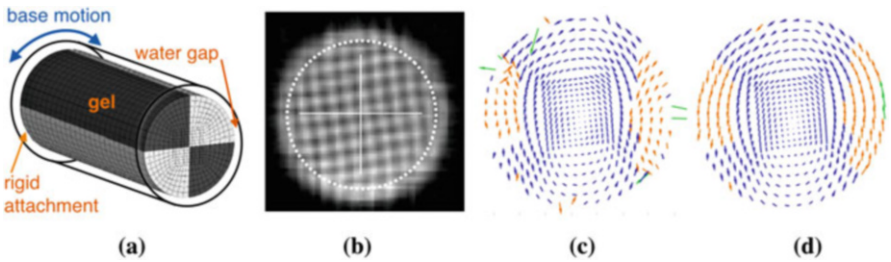

Fig. 1 Acceleration-induced brain phantom deformation. As shown in the schematic (**a**), motion of the base causes deformation into a new configuration (**b**). Conventional HARP analysis (**c**) shows large-displacement artifacts (*orange*), and spurious displacements at the edges (*green*). The problematic areas in proposed method (**d**) are largely artifact-free

modeled prestretch via interstitial growth [19], and (b) evaluate changes in tracking results due to prestretch-induced stiffness variations. To this end, the left ventricle of a healthy volunteer was imaged (3T scanner, 12 long slices, eight long slices, 256 ×256, 1.25 ×1.25 mm, CSPAMM sequence), and images at early diastole (lowest pressure load) were used to generate an FE model consisting of 6500 linear brick elements. Simulated contraction, with parameters available in [1, 18], was used as ground truth displacements, and to create synthetic deformed images for tracking.

Two displacement results were obtained with a stress-free reference (SFR) and a prestretched reference (PSR), which included −5\% mean fiber prestretch [18, 19]. In both, tracking was performed to $\varepsilon = 0.2$ rad. Tracking from SFR terminated after 17 iterations using $\lambda_{\max} = 0.2 \times 10^{-2}$ and $\lambda_{\text{tol}} = 5 \times 10^{-2}$. The same values for PSR after ten iterations were 1.4×10^{-2} and 7×10^{-2}, respectively. Compared to the ground truth, the displacement residuals were 0.6±0.3 mm and 0.9±0.3 mm (SFR and PSF, respectively). This similarity in residuals shows that prestretch-induced variations can be compensated by tracking parameters. Thus, although the image-derived deformed configurations are similar, the PSF relates to a reference state consistent with experimental evidence of residual stress, Fig. 2(a), and results in visibly higher systolic fiber shortening, Fig. 2(b) and (c).

4.3 Estimating Activation of Intrinsic Tongue Muscles

In this experiment, we estimate the magnitude of activation stress responsible for an observed deformation in the tongue. To this end, motion was first tracked based on a stack of images from a healthy volunteer at two time frames (3T scanner, ten coronal slices, eight sagittal slices, 256×256, 1.9×1.9 mm, CSPAMM

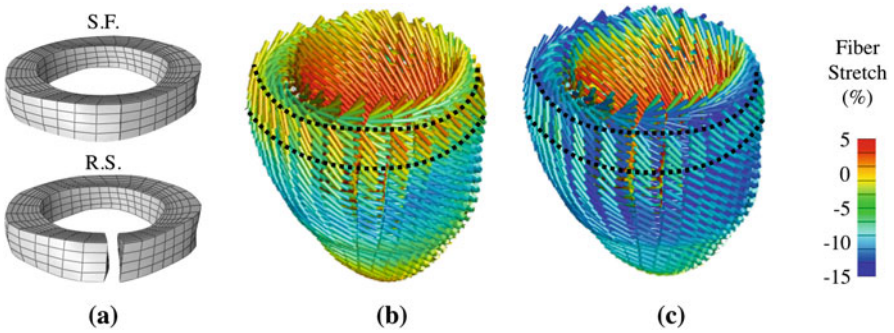

Fig. 2 Comparison between SFR and PSR. A radial cut (**a**) on a ring-like section shows no change in the SFR, but the same cut causes separation of edges in the PSR, similar to experimental observations [18]. Comparable deformed configurations exhibit different fiber stretches with respect to the SFR (**b**) or the PSR (**c**)

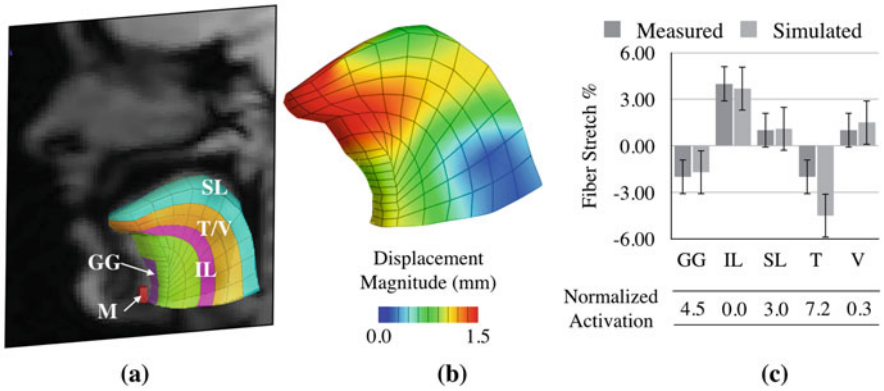

Fig. 3 Motion estimation in the tongue. Five muscles from MRI (**a**) are used within an FE model to extract deformations (**b**), and to simulate activation stresses. Measured and simulated fiber stretches (**c**) show qualitative agreement with those extracted from the tagged images. Key: *GG* genioglossus, *IL* inferior longitudinal, *SL* superior longitudinal, *T* transverse, *V* verticalis *M* mandible insertion

sequence) using an FE model consisting of 280 quadratic brick elements, and the tracking constraint set to $\varepsilon = 0.05$ rad. To obtain contractile stress normalized to material stiffness, the tissue was modeled as a Neo-Hookean solid ($C_1 = 1.0$ kPa, $\kappa = 120$ kPa). Fiber directionality and muscle definitions were based on the literature [7]. Unlike previous work, which relied on numerical optimization—where multiple simulations were run to find the closest match between simulated and observed tongue deformation—our strategy was to directly approximate the contractile stresses from the image-derived fiber shortening according to the active contraction model presented in [1] (solving for $T_{\max}$ in Eq. 4). These approximations were applied uniformly over each of the muscles in Fig. 3(a).

Image tracking, the basis of the observed tongue deformation, terminated after ten iterations $\lambda_{\max} = 1.0$ and $\lambda_{\text{tol}} = 0.1$. Displacement results appear in Fig. 3b. Experimental and simulated fiber stretches averaged over the muscle region appear in Fig. 3c, and show qualitative agreement. Comparison between the image-based deformation and activation simulation allows direct estimation of contractile stress, avoiding numerical optimization, which may converge at local minima [7]. Note that both, forward simulations and image tracking via the proposed phase tracking constraint, occur in the same geometrical model; thus, comparison between experimental and simulated behavior can be done on an element-per-element basis.

5 Discussion

This study extends fundamental concepts used for motion estimation based on scalar intensity images to the vectorial phase domain, which allows application of tagged images for mechanically regularized motion estimation. One immediate

advantage of this type of regularization is the reduction of artifacts present at the edges where image information is affected by partial volume. The use of tagged images disambiguates similarity metrics associated with intensity in areas of low texture. This improves motion tracking, and adds robustness to material parameter uncertainty.

As shown in previous literature featuring intensity-based motion estimation in FE models [1], displacements can be made consistent despite changes in material parameters by scaling the tracking penalty. The idea is that, within a range, a stiffer material will simply require larger forces to produce the same deformation. In the proposed method, we take advantage of the vectorial nature of phase to extract a similarity metric, ε, that serves as a stopping criteria for motion estimation; the tracking penalty continues to be scaled until the criteria is met. This basic principle was demonstrated when tracking deformation in residually stressed ventricular tissue, where the tracking parameters associated with the PSR were much larger than the SFR, even though the tracking metric and displacement accuracy were identical.

In terms of implementation, the proposed method effectively reduces to calculating body forces derived from phase images, i.e., the application of nodal forces where each (xyz) component is equal to scaled differences between template and target phase image in each corresponding tagging direction. The stiffness contribution, evaluated once per element, is defined similarly to the contribution of the material model but is defined as described in (6). From an image processing standpoint, upsampling of images enables the use of advantageous interpolation techniques that would be computationally expensive to evaluate along with the FE tracking constraint.

6 Conclusion

The main goal of this paper was to introduce and demonstrate unique features associated with this motion estimation strategy, including artifact reduction, robustness to material parameters, and interaction between observed motion and mechanical features like realistic geometry and fibers. Future research directions will focus on the relative performance of its different components, both from an imaging standpoint (the effects of image quality, upsampling, and filtering) and from a modeling perspective (the consequences of constitutive modeling and geometrical representation), and with respect to other motion estimation techniques.

Acknowledgments This research was funded by NIH Grant R01-NS055951, supplement PA12-149, and support by the Center for Neuroscience and Regenerative Medicine.

References

1. Phatak NS, Maas SA, Veress AI, Pack NA, Di Bella EVR, Weiss JA (2009) Strain measurement in the left ventricle during systole with deformable image registration. Med Image Anal 13:354–361
2. Wright RM, Ramesh KT (2012) An axonal strain injury criterion for traumatic brain injury. Biomech Model Mechanobiol 11:245–260
3. Haber I, Metaxas DN, Axel L (2000) Three-dimensional motion reconstruction and analysis of the right ventricle using tagged MRI. Med Image Anal 4:335–355
4. Ibrahim E-SH (2011) Myocardial tagging by cardiovascular magnetic resonance: evolution of techniques-pulse sequences, analysis algorithms, and applications. J Cardiovasc Magn Reson 13:36
5. Bayly PV, Clayton EH, Genin GM (2012) Quantitative imaging methods for the development and validation of brain biomechanics models. Annu Rev Biomed Eng 14:369–396
6. Moerman KM, Sprengers AMJ, Simms CK, Lamerichs RM, Stoker J, Nederveen AJ (2012) Validation of tagged MRI for the measurement of dynamic 3D skeletal muscle tissue deformation. Med Phys 39:1793–1810
7. Harandi, N.M., Woo, J., Farazi, M.R., Stavness, L., Stone, M., Fels, S., Abugharbieh, R. (2015) Subject-specific biomechanical modelling of the oropharynx with application to speech production. IEEE ISBI, pp 1389–1392
8. Knutsen AK, Magrath E, McEntee JE, Xing F, Prince JL, Bayly PV, Butman JA, Pham DL (2014) Improved measurement of brain deformation during mild head acceleration using a novel tagged MRI sequence. J Biomech 47:3475–3481
9. Spottiswoode BS, Zhong X, Hess AT, Kramer CM, Meintjes EM, Mayosi BM, Epstein FH (2007) Tracking myocardial motion from cine DENSE images using spatiotemporal phase unwrapping and temporal fitting. IEEE Trans Med Imaging 26:15–30
10. Liu X, Abd-Elmoniem KZ, Stone M, Murano EZ, Zhuo J, Gullapalli RP, Prince JL (2012) Incompressible deformation estimation algorithm (IDEA) from tagged MR images. IEEE Trans Med Imaging 31:326–340
11. Osman NF, McVeigh ER, Prince JL (2000) Imaging heart motion using harmonic phase MRI. IEEE Trans Med Imaging 19:186–202
12. Horn, B.K., Schunck, B.G. (1981) Determining optical flow. In: Technical Eymposium East. pp. 319–331
13. Bonet J, Wood RD (1997) Nonlinear continuum mechanics for finite element analysis. Cambridge University Press, Cambridge
14. Bathe KJ (1996) Finite element procedures. Prentice-Hall, Upper Saddle River
15. Maas SA, Ellis BJ, Ateshian GA, Weiss JA (2012) FEBio: finite elements for biomechanics. J Biomech Eng 134(1):011005
16. Spencer AJM (1985) Continuum mechanics. Dover Books, Essex
17. Guo H, Nickel JC, Iwasaki LR, Spilker RL (2012) An augmented Lagrangian method for sliding contact of soft tissue. J Biomech Eng 134:084503
18. Genet M, Rausch MK, Lee LC, Choy S, Zhao X, Kassab GS, Kozerke S, Guccione JM, Kuhl E (2015) Heterogeneous growth-induced prestrain in the heart. J Biomech 48:2080–2089
19. Ateshian GA, Ricken T (2010) Multigenerational interstitial growth of biological tissues. Biomech Model Mechanobiol 9:689–702